# Remote Coordination Adjustment of Power Electronic Devices in AC/DC Systems by Power Flow Calculation with Linearization and Sensitivity

Junzhou Wang, Xingyu Lin, Junjie Tang, Yuzhi Wang, Guodong Huang, and Dan Xu

***Abstract*—High proportion of renewable energies and the installation of power electronic devices (PEDs) pose tough challenges to the operation of power systems. In this paper, the remote coordination adjustment (RCA) of PEDs in stochastic scenarios is studied. The steady-state model for the AC/DC system with PEDs is first established, and the alternate iteration method based on linearization (AIML) is adopted, especially for efficient deterministic power flow calculation. Then, the RCA is proposed using a modular local sensitivity method combined with AIML, which can adjust the electrical variables by diverse PEDs with high efficiency. Additionally, the probabilistic power flow calculation using the quasi-Monte Carlo method with the adaptive sampling number (ASN-QMC) is introduced to keep the balance between the computational efficiency and accuracy, as well as demonstrating the positive impact of RCA by the PEDs in stochastic scenarios. The effectiveness of the proposed RCA is validated by a series of modified IEEE test systems.**

***Index Terms*—Power electronic device, remote coordination adjustment (RCA), AC/DC system, linearization, sensitivity, uncertainty, power flow, quasi-Monte Carlo.**

## I. Introduction

With the continuous expansion of the power system scale, challenges related to the increasing integration of renewable energies and installation of power electronic devices (PEDs) have garnered significant attention. The large-scale integration of renewable energies introduces significant randomness, potentially increasing the fault probability in critical areas in the power system, thus leading to widespread power outages [1]. Additionally, benefiting from the fast development of materials and control technology, PEDs have been more widely applied in power systems [2], [3], requiring more judicious operation of these devices to ensure the secure operation of the system. In the context of the power system characterized by a high proportion of renewable energy integration and PED installation, several critical challenges emerge: ① the efficiency and accuracy of deterministic power flow (DPF) calculation on such system with PEDs must be well balanced; ② the accuracy and efficiency of such system state determination with large-scale uncertainties should be ensured; and ③ PEDs can be coordinated to mitigate the risk of out-of-limit in some critical areas in stochastic scenarios.

PEDs are primarily used in high-voltage direct current (HVDC) transmission system and flexible AC transmission system (FACTS). The voltage source converter (VSC) is widely used in HVDC, offering advantages such as independent control of active/reactive power and the ability to provide the reverse current without changing the voltage polarity [4]. The studies of AC/DC system based on voltage source converter based high-voltage direct current (VSC-HVDC) have continuously increased in recent years [5], [6]. The FACTS includes the unified power flow controller (UPFC), generalized UPFC (GUPFC), static synchronous compensator (STATCOM), static synchronous series compensator (SSSC), etc., which possess various functionalities: voltage regulation, series compensation, power control, phase shift and so forth [7]. Given their ability to control the electrical variables in the power system flexibly, the PEDs provide a new option to guarantee the secure operation of power systems [8].

To reveal the impact of PEDs on power system operation, it is crucial to conduct the DPF calculation of the AC/DC system with PEDs. The DPF calculation methods can be divided into the alternate iteration method (AIM) and the unified iteration method (UIM). AIM possesses a clear physical meaning, reduced computational burden per module, and ease of programming. In [9] and [10], AIM is adopted for

Manuscript received: July 23, 2024; revised: January 3, 2025; accepted: March 24, 2025. Date of CrossCheck: March 24, 2025. Date of online publication: April 25, 2025.

This work was supported by the National Natural Science Foundation of China (No. 52177071).



J. Wang, X. Lin, J. Tang (corresponding author), and Y. Wang are with State Key Laboratory of Power Transmission Equipment Technology, School of Electrical Engineering, Chongqing University, Chongqing, China (e-mail: wangjunzhou@cqu. edu. cn; linxingyu@cqu. edu. cn; tangjunjie@cqu. edu. cn; wangyuzhi@cqu.edu.cn).

G. Huang and D. Xu are with the Beijing Key Laboratory of Research and System Evaluation of Power Dispatching Automation Technology, China Electric Power Research Institute, Beijing, China (e-mail: hgd2088@126. com; xudan@epri.sgcc.com.cn).

DOI: 10.35833/MPCE.2024.000784

the power flow calculation of the AC/DC system. However, only limited research works have explored the use of AIM for DPF of AC/DC systems with different kinds of PEDs. Based on the Newton-Raphson method, UIM is widely used due to its strong convergence properties. The steady-state models of the system with PEDs have been established and solved using UIM in [11]-[13]. To alleviate the computational cost of nonlinear power flow equations in UIM, the linearization methods can be applied [14], [15]. In [15], the results show that the adopted method improves the efficiency of the DPF calculation. However, identifying a linearization strategy is time-consuming, and large changes in the inputs necessitate a new linearization strategy. While linearization methods increase computational speed, they yield approximate results with some inherent uncertainty in calculation accuracy. Moreover, the modeling of PEDs in DPF above focuses solely on the fact that PEDs can control the electrical variables of their locations, i. e., the so-called local adjustment of PEDs, thus neglecting their remote coordination adjustment (RCA) to mitigate risks in the critical areas.

To consider the coordination support ability of PEDs in managing remote electrical variables and mitigating associated risk, the optimal power flow (OPF) calculation and sensitivity method can be used. OPF achieves the optimal objectives by adjusting the control quantities under the specific constraints of the system, leading to a great computational burden. References [16]-[19] focus on the OPF of the system with PED adjustments while employing such approximate or equivalent methods to alleviate the computational complexity. The sensitivity method uses local sensitivity to delineate the local linear relationships amongst variables, guiding the adjustment of control variables. Notably, this method primarily focuses on adjusting the target output, making it computationally efficient and ideal for real-time calculation [20]. Reference [21] studies the real-time system redispatch by PEDs based on injected voltage source formulation and the optimal location for PED installation using the equivalent impedance formulation by the sensitivity method. In [22], one control parameter of a single UPFC is considered to remotely adjust the active power loops by the sensitivity method, which limits the full utilization of the RCA ability of multiple PEDs.

To reveal the out-of-limit in critical areas with large-scale uncertainties, the probabilistic power flow (PPF) method is generally adopted, including three main categories: analytical method, approximate method, and Monte Carlo simulation (MCS) method [23]. The MCS method generates the samples according to the probability distribution of input, and obtains the probability characteristics of the output through a lot of DPF calculations. Compared with the analytical and approximate methods, the MCS method can get the probability distribution of output more accurately, especially for the tail parts. With sufficient samples (always a large number of samples), the MCS method based on random sampling (RS-MCS) is of great robustness, and the results are generally used as a reference for other PPF methods. At the same time, RS-MCS suffers from a computational burden [24]. To improve the computational efficiency of RS-MCS, the MCS method based on Latin hypercube sampling (LHS-MCS) is widely used [24]-[26]. However, the samples from LHS-MCS show stratification only in unidimensional space. Still, they may not be uniformly distributed in high dimensions, thus requiring more samples for accuracy, i.e., greater computational burden. Many studies aim to improve the uniformity of high-dimensional LHS-MCS samples [27]-[29]. However, they do not get rid of the curse of dimensionality for the high-dimensional problems. Besides, the sampling number is determined and fixed using the traditional LHS-MCS method. Thus, the re-sampling must be conducted when the sampling number is insufficient to satisfy the accuracy requirement. To solve this problem, the inherited LHS technique is proposed [30]. However, this method only doubles the sampling number per change, which is inflexible. The sample uniformity obtained by the quasi-Monte Carlo (QMC) method is proved to be better than that by the LHS-MCS method [31]. In [32], the QMC method is applied to the PPF calculation. And in [33], the extended QMC is proposed to find the appropriate sampling number freely. However, the method in [33] is only applied in the pure AC system with limited efficiency gains because the DPF of a pure AC system is less time-consuming. Moreover, many studies focus solely on the system state analysis using the PPF, neglecting risk mitigation adjustments.

To overcome the above issues, this paper studies RCA of PEDs in AC/DC system by power flow calculation with linearization and sensitivity in stochastic scenarios. The main contributions are summarized as follows.

1) The DPF of the AC/DC system with PEDs is calculated through the alternate iteration method based on linearization (AIML). This method linearizes the power flow equations of each module for acceleration. Different from the traditional linearization method, the convergence criterion is adopted to ensure accuracy.

2) The RCA of PEDs is proposed, which performs one iteration of AIML first, then adjusts PEDs by the modular local sensitivity, and satisfies the convergence criterion of DPF and adjustment. This strategy enables PEDs to adjust the target value in critical areas, i.e., the active power of tie lines, where PEDs are non-adjacent.

3) The QMC method with an adaptive sampling number (ASN-QMC) is introduced to calculate the PPF of the AC/DC system with PEDs and reveal the positive effect of such non-adjacent PEDs on improving the grid operation security. This method inherits the advantages of QMC, which adaptively selects the appropriate sampling number, thus achieving efficiency.

The rest of this paper is organized as follows. The modeling of the AC/DC system with PEDs and the DPF solution using AIML is introduced in Section II. The RCA by PEDs is presented in Section III. The ASN-QMC for RCA by PEDs in stochastic scenarios is introduced in Section IV. In Section V, several test cases are designed and studied. Section VI concludes this paper.

## II. Modeling of AC/DC System with PEDs and DPF Solution Using AIML

### A. Steady-state Modeling of AC/DC System with PEDs

#### 1) PED

The equivalent circuit of VSC station, GUPFC (or UPFC), STATCOM, and SSSC are shown in Supplementary Material A Fig. SA1. The steady-state model of VSC station considers the losses associated with power exchange, whereas the other models for GUPFC (or UPFC), SSSC, and STATCOM neglect the power losses. The mismatch equations of PEDs in Supplementary Material A (A1)-(A4) can be simplified as (1), and the detailed definitions of each variable can be found in Supplementary Material A.

$$\begin{cases} \boldsymbol{F}_{VSC}=\boldsymbol{f}_{VSC}(\boldsymbol{x}_{VSC})=\boldsymbol{0} & \text{VSC station} \\ \boldsymbol{F}_{GUPFC}=\boldsymbol{f}_{GUPFC}(\boldsymbol{x}_{GUPFC})=\boldsymbol{0} & \text{GUPFC} \\ \boldsymbol{F}_{STATCOM}=\boldsymbol{f}_{STATCOM}(\boldsymbol{x}_{STATCOM})=\boldsymbol{0} & \text{STATCOM} \\ \boldsymbol{F}_{SSSC}=\boldsymbol{f}_{SSSC}(\boldsymbol{x}_{SSSC})=\boldsymbol{0} & \text{SSSC} \end{cases} \tag{1}$$

#### 2) AC System

The power flow mismatch equations of AC bus $i$ are:

$$\begin{cases} \Delta P_i=P_i-\mathrm{Re}\left\{\sum_j \dot{V}_i[(\dot{V}_i-\dot{V}_j)Y_{ij}]^*\right\}=0 \\ \Delta Q_i=Q_i-\mathrm{Im}\left\{\sum_j \dot{V}_i[(\dot{V}_i-\dot{V}_j)Y_{ij}]^*\right\}=0 \end{cases} \tag{2}$$

where $\Delta P_i$ and $\Delta Q_i$ are the active and reactive power mismatches of bus $i$, respectively; $\dot{V}_i$ and $\dot{V}_j$ are the voltages of buses $i$ and $j$, respectively; $Y_{ij}$ is the $i^{\text{th}}$-row $j^{\text{th}}$-column element in the AC bus admittance matrix; and $P_i$ and $Q_i$ are the active and reactive power injections on bus $i$ (sourced from the load, generator, and power injection from PEDs), respectively. Equation (2) can be simplified as:

$$\boldsymbol{F}_{ac}=\boldsymbol{f}_{ac}(\boldsymbol{x}_{ac})=\boldsymbol{0} \tag{3}$$

where $\boldsymbol{F}_{ac}=[\Delta P,\Delta Q]^{\mathrm{T}}$, and $\Delta P$ and $\Delta Q$ are the active and reactive mismatch power equations, respectively; $\boldsymbol{f}_{ac}$ is the vector of mismatch equations of the AC system; and $\boldsymbol{x}_{ac}$ is the vector of bus voltages of AC system.

#### 3) DC System

The mismatch equation of the DC system $\Delta P_{dc,i}$ is given as [34]:

$$\Delta P_{dc,i}=P_{Gdc,i}-P_{Ldc,i}+P_{c,dc,i}-V_{dc,i}\sum_j V_{dc,j}Y_{dc.ij}=0 \tag{4}$$

where $V_{dc,i}$ is the voltage of DC bus $i$; $Y_{dc,ij}$ is the $i^{\text{th}}$-row $j^{\text{th}}$-column element in the conductance matrix; $P_{Gdc,i}$ and $P_{Ldc,i}$ are the active power of generator and load on DC bus $i$, respectively; and $P_{c,dc,i}$ is the power flowing from VSC to DC bus $i$. Equation (4) can be simplified:

$$\boldsymbol{F}_{dc}=\boldsymbol{f}_{dc}(\boldsymbol{x}_{dc})=\boldsymbol{0} \tag{5}$$

where $\boldsymbol{F}_{dc}=[\Delta P_{dc,1},\Delta P_{dc,2},\ldots]^{\mathrm{T}}$; $\boldsymbol{f}_{dc}$ is the vector of mismatch equations of the DC system; and $\boldsymbol{x}_{dc}$ is the vector of bus voltages of the DC system.

### B. Procedure of AIML for AC/DC System with PEDs

#### 1) Basic Concept of Linearization

The equation to be solved is $\boldsymbol{F}(\boldsymbol{x})=\boldsymbol{f}(x_1,x_2,\ldots)=\boldsymbol{0}$, where $\boldsymbol{F}$ is a multivariate function with $\boldsymbol{x}=[x_1,x_2,\ldots]$ as the state variable, namely bus voltage magnitude $V$ and phase angle $\theta$.

The linearized equation of $\boldsymbol{F}(\boldsymbol{x})$ at linearized variable $\phi(\boldsymbol{x}_0)$ about a specific value $\boldsymbol{x}_0$ for linearized variable $\phi(\boldsymbol{x})$ can be obtained by preserving the first-order term of its Taylor expansion:

$$\boldsymbol{F}\approx \boldsymbol{F}(\boldsymbol{x})\big|_{\boldsymbol{x}_0}+\left.\frac{\partial \boldsymbol{F}(\boldsymbol{x})}{\partial \phi(\boldsymbol{x})}\right|_{\boldsymbol{x}_0}(\phi(\boldsymbol{x})-\phi(\boldsymbol{x}_0)) \tag{6}$$

For the linearized variable $\phi(\boldsymbol{x})$, there are three typical forms, and their state variables are given as [35]:

$$\phi(\boldsymbol{x})=(\varphi(V),\eta(\theta))=(V,\theta),\ (V^2,\theta),\ \text{or}\ (\ln V,\theta) \tag{7}$$

where $\varphi(V)$ and $\eta(\theta)$ denote different forms of $V$ and $\theta$, respectively.

The value of $\left.\frac{\partial \boldsymbol{F}(\boldsymbol{x})}{\partial \phi(\boldsymbol{x})}\right|_{\boldsymbol{x}_0}$ in (6) can be calculated as:

$$\frac{\partial \boldsymbol{F}(\boldsymbol{x})}{\partial \phi(\boldsymbol{x})}=\frac{\partial \boldsymbol{F}(\boldsymbol{x})}{\partial \boldsymbol{x}}\frac{\partial \boldsymbol{x}}{\partial \phi(\boldsymbol{x})}=\frac{\partial \boldsymbol{F}(\boldsymbol{x})}{\partial \boldsymbol{x}}\frac{\partial \phi^{-1}(\phi(\boldsymbol{x}))}{\partial \phi(\boldsymbol{x})} \tag{8}$$

From (8), $\partial \boldsymbol{F}(\boldsymbol{x})/\partial \boldsymbol{x}$ is calculated first, and $\partial \phi^{-1}(\phi(\boldsymbol{x}))/\partial \phi(\boldsymbol{x})$ can be determined according to different linearization types in (7). In the following linearization strategy, the form $(V,\theta)$ is adopted due to its brevity and low computational burden [35].

#### 2) Calculation Procedure of AIML

The mismatch equations (1), (3), and (5) are linearized by (6). The calculation procedure of AIML for the AC/DC system with PEDs is outlined as follows.

*Step 1*: import the system data and set the initial values.

*Step 2*: linearize the mismatch equations of each module of PEDs, and then calculate the power flow. Note that each module is independent, and parallel computations can be performed (not applied in this paper).

*Step 3*: calculate the power injection flowing from PEDs into the AC system. Linearize the mismatch equations of the AC system, and calculate the power flow distribution.

*Step 4*: determine the power injection flowing from the VSC station into the DC system. Linearize the mismatch equations of the DC system, and calculate the power flow distribution.

*Step 5*: update the bus voltage of the AC/DC system.

*Step 6*: judge whether two iterations (the $k^{\text{th}}$ and $(k-1)^{\text{th}}$) satisfy the convergence criterion of DPF.

$$\max\left|\boldsymbol{\chi}^{(k)}-\boldsymbol{\chi}^{(k-1)}\right|<\varepsilon_{AIML} \tag{9}$$

where $\boldsymbol{\chi}$ denote all the state variables in the system, including the bus voltage of the AC/DC system and PEDs; superscript $(k)$ represents the $k^{\text{th}}$ iteration; and $\varepsilon_{AIML}$ is the convergence coefficient of DPF, and usually, $\varepsilon_{AIML}=10^{-6}$. If the convergence criterion in (9) is not satisfied, repeat *Step 2* to *Step 6*, or calculate other required data and output the results.

Linearization is only applied to the nonlinear equations in AIM without changing the procedure or the convergence criterion. Therefore, the accuracy of AIML is consistent with that of AIM. For each iteration, the diagrams of three different methods (UIM, AIM, and AIML) are shown in Fig. 1.

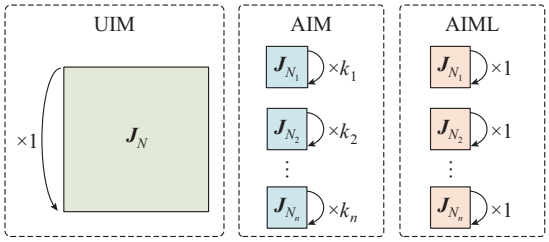


Fig. 1. Diagrams of three different methods for each iteration.

In Fig. 1, $\boldsymbol{J}_{N_x}$ is the Jacobian matrix, and $N_x$ denotes the matrix dimension. The larger the $N_x$ of the Jacobian matrix is, the greater the computational burden required for solving the mismatch equations. If the mismatch equations are solved by inverting $\boldsymbol{J}_{N_x}$, the time complexity for the inverse matrix is known to be $O(N_x^3)$. And it is easy to prove: $\boldsymbol{J}_N$ is more computationally complex than $\boldsymbol{J}_{N_1}, \boldsymbol{J}_{N_2}, \ldots, \boldsymbol{J}_{N_n}$ combined, especially as $N$ increases. UIM requires a Jacobian matrix with all the variables for each iteration. For AIM, although the whole system is divided into several modules, the Jacobian matrix of each module still needs to be calculated repeatedly to satisfy its convergence criterion. Therefore, it is hard to state whether AIM or UIM has a higher computational efficiency. Similar to AIM, AIML is divided into several modules, but each module of AIML is equivalent to performing only a single Jacobian matrix calculation. As a result, the computational efficiency of the three methods for each iteration can be ranked as: AIML > AIM ≈ UIM.

## III. RCA BY PEDS

### A. Solving Local Sensitivity Method

To perform RCA by PEDs, it is necessary to calculate the local sensitivity matrix $\boldsymbol{S}_{\boldsymbol{u}}^{\boldsymbol{y}}$ of the target output $\boldsymbol{y}$ (e.g., the active power of tie lines) with respect to the control parameters $\boldsymbol{u}$ of PEDs.

#### 1) Traditional Local Sensitivity

The local sensitivity matrix using a traditional solution $\boldsymbol{S}_{\boldsymbol{Tu}}^{\boldsymbol{y}}$ directly considers the coupling relationship of the whole system in one equation. The target output $\boldsymbol{y}$ is affected by the state variables $\boldsymbol{\chi}$ and $\boldsymbol{u}$, and hence $\boldsymbol{y}$ can be expressed as $\boldsymbol{y} = \boldsymbol{y}(\boldsymbol{\chi}, \boldsymbol{u})$. The power flow equation for the whole system is given as:

$$\boldsymbol{f}_w(\boldsymbol{\chi}, \boldsymbol{u}) = \boldsymbol{0} \tag{10}$$

where $\boldsymbol{f}_w$ is the mismatch equation of the whole system.

The traditional local sensitivity $\boldsymbol{S}_{\boldsymbol{Tu}}^{\boldsymbol{y}}$ can be obtained as:

$$\boldsymbol{S}_{\boldsymbol{Tu}}^{\boldsymbol{y}} = \frac{\partial \boldsymbol{y}}{\partial \boldsymbol{u}^{\mathrm{T}}} - \frac{\partial \boldsymbol{y}}{\partial \boldsymbol{\chi}^{\mathrm{T}}} \left( \frac{\partial \boldsymbol{f}_w}{\partial \boldsymbol{\chi}^{\mathrm{T}}} \right)^{-1} \frac{\partial \boldsymbol{f}_w}{\partial \boldsymbol{u}^{\mathrm{T}}} \tag{11}$$

#### 2) Modular Local Sensitivity

The local sensitivity matrix can be also calculated using modular local sensitivity $\boldsymbol{S}_{\boldsymbol{Mu}}^{\boldsymbol{y}}$. The modular local sensitivity relies on the intermediate variable, i. e., the active/reactive power injections of each bus (sourced from the load, generator, and PEDs), as a bridge, indirectly considering the linear relationship between the modules. The relationship between $\boldsymbol{y}$ and $\boldsymbol{u}$ can be represented as:

$$\begin{cases} \Delta \boldsymbol{y} = \dfrac{\partial \boldsymbol{y}}{\partial \boldsymbol{u}^{\mathrm{T}}} \Delta \boldsymbol{u} - \dfrac{\partial \boldsymbol{y}}{\partial \boldsymbol{\chi}^{\mathrm{T}}} \left( \dfrac{\partial \boldsymbol{x}}{\partial \boldsymbol{u}^{\mathrm{T}}} \Delta \boldsymbol{u} + \boldsymbol{S}_{\boldsymbol{s}}^{\boldsymbol{u}} \Delta \boldsymbol{s} \right) = \\ \quad \dfrac{\partial \boldsymbol{y}}{\partial \boldsymbol{u}^{\mathrm{T}}} \Delta \boldsymbol{u} - \dfrac{\partial \boldsymbol{y}}{\partial \boldsymbol{\chi}^{\mathrm{T}}} \left[ \dfrac{\partial \boldsymbol{x}}{\partial \boldsymbol{u}^{\mathrm{T}}} \Delta \boldsymbol{u} + \boldsymbol{S}_{\boldsymbol{s}}^{\boldsymbol{u}} \left( \dfrac{\partial \boldsymbol{s}}{\partial \boldsymbol{u}^{\mathrm{T}}} \Delta \boldsymbol{u} + \dfrac{\partial \boldsymbol{s}}{\partial \boldsymbol{v}^{\mathrm{T}}} \boldsymbol{S}_{\boldsymbol{u}}^{\boldsymbol{v}} \Delta \boldsymbol{u} \right) \right] = \\ \quad \left\{ \dfrac{\partial \boldsymbol{y}}{\partial \boldsymbol{u}^{\mathrm{T}}} - \dfrac{\partial \boldsymbol{y}}{\partial \boldsymbol{\chi}^{\mathrm{T}}} \left[ \dfrac{\partial \boldsymbol{\chi}}{\partial \boldsymbol{u}^{\mathrm{T}}} + \boldsymbol{S}_{\boldsymbol{s}}^{\boldsymbol{u}} \left( \dfrac{\partial \boldsymbol{s}}{\partial \boldsymbol{u}^{\mathrm{T}}} + \dfrac{\partial \boldsymbol{s}}{\partial \boldsymbol{v}^{\mathrm{T}}} \boldsymbol{S}_{\boldsymbol{u}}^{\boldsymbol{v}} \right) \right] \right\} \Delta \boldsymbol{u} = \boldsymbol{S}_{\boldsymbol{Mu}}^{\boldsymbol{y}} \Delta \boldsymbol{u} \\ \boldsymbol{S}_{\boldsymbol{s}}^{\boldsymbol{u}} = -\left( \dfrac{\partial \boldsymbol{f}_{ac}}{\partial \boldsymbol{u}^{\mathrm{T}}} \right)^{-1} \dfrac{\partial \boldsymbol{f}_{ac}}{\partial \boldsymbol{s}^{\mathrm{T}}} \\ \boldsymbol{S}_{\boldsymbol{u}}^{\boldsymbol{v}} = -\left( \dfrac{\partial \boldsymbol{f}_{PED}}{\partial \boldsymbol{v}^{\mathrm{T}}} \right)^{-1} \dfrac{\partial \boldsymbol{f}_{PED}}{\partial \boldsymbol{u}^{\mathrm{T}}} \end{cases} \tag{12}$$

where $\boldsymbol{v}$ is the vector of bus voltages of PEDs; $\Delta \boldsymbol{u}$ and $\Delta \boldsymbol{s}$ denote the changes in state variable $\boldsymbol{u}$ and sensitivity variable $\boldsymbol{s}$; and $\boldsymbol{f}_{PED}$ is the vector of mismatch equations of PEDs.

Actually, the computational burden of calculating $\boldsymbol{S}_{\boldsymbol{u}}^{\boldsymbol{y}}$ ($\boldsymbol{S}_{\boldsymbol{Tu}}^{\boldsymbol{y}}$ and $\boldsymbol{S}_{\boldsymbol{Mu}}^{\boldsymbol{y}}$) primarily depends on the inverse matrix calculation. If UIM is adopted, the inverse matrix in $\boldsymbol{S}_{\boldsymbol{Tu}}^{\boldsymbol{y}}$ has been calculated, making the traditional local sensitivity more suitable. When AIML is employed, the inverse matrices in $\boldsymbol{S}_{\boldsymbol{s}}^{\boldsymbol{u}}$ and $\boldsymbol{S}_{\boldsymbol{u}}^{\boldsymbol{v}}$ in $\boldsymbol{S}_{\boldsymbol{Mu}}^{\boldsymbol{y}}$ have been calculated in each module, indicating that the modular local sensitivity is more suitable.

### B. Procedure of RCA by PEDs

The schematic diagram of RCA by PEDs is shown in Fig. 2. Compared with local adjustment, PEDs are non-adjacent to the tie lines, necessitating the design of the adjustment strategy by PEDs to modify the active power of the tie lines.

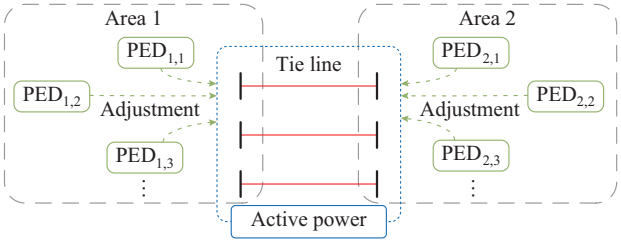


Fig. 2. Schematic diagram of RCA by PEDs.

There are two primary methods to perform RCA, summarized as Π-out [22] and Π-in, where Π denotes the AIM, UIM, AIML or any other iteration solution methods for DPF. The procedure of Π-out is: perform a DPF to satisfy the convergence criterion of the DPF, followed by adjusting PEDs to satisfy the convergence criterion of adjustment. The procedure of Π-in is given as: perform one iteration in DPF, followed by adjusting PEDs, which satisfies the convergence criterion of both DPF and the adjustment. The differences between Π-out and Π-in are depicted in Fig. 3. Six methods can be used to perform RCA: UIM-in, AIM-in, AIML-in, UIM-out, AIM-out, and AIML-out.

In this paper, AIML-in is adopted to perform RCA by PEDs. The procedure using modular local sensitivity is outlined as follows.

*Step 1*: import system data and set the target value of the active power $P_{\mathrm{t},(i_k\text{-}j_k)}^{ref}$ of tie line $i_k$-$j_k$.

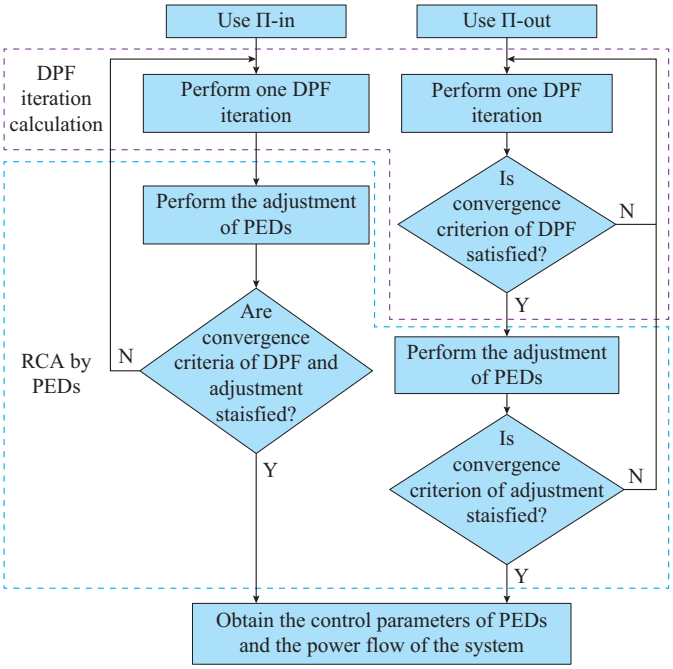


Fig. 3. Differences between Π-out and Π-in.

*Step 2*: perform one DPF iteration calculation of AIML, and then calculate $\boldsymbol{S}_{Mu}^{y}$.

*Step 3*: determine the target value $\boldsymbol{y}$.

$$\boldsymbol{y}=\sum_{k=1}^{n_{\mathrm{t}}}\left|P_{\mathrm{t}(i_k\text{-}j_k)}-P_{\mathrm{t}(i_k\text{-}j_k)}^{ref}\right| \tag{13}$$

where $P_{\mathrm{t}(i_k\text{-}j_k)}$ is the current value of the active power of tie line $i_k$-$j_k$; and $n_{\mathrm{t}}$ is the number of tie lines. Since the target is $\boldsymbol{y}=\boldsymbol{0}$, the difference from the target $\boldsymbol{y}$ is $\Delta\boldsymbol{y}=\boldsymbol{0}-\boldsymbol{y}=-\boldsymbol{y}$.

*Step 4*: $\Delta\boldsymbol{y}$ and $\Delta\boldsymbol{u}$ satisfy $\Delta\boldsymbol{y}=\boldsymbol{S}_{Mu}^{y}\Delta\boldsymbol{u}$. Since the dimension of $\boldsymbol{u}$ is always greater than or equal to that of $\boldsymbol{y}$, the minimum norm solution is obtained through the pseudo-inverse calculation, yielding the minimum change $\Delta\boldsymbol{u}^{(k)}$ of the control parameters of PED for the $k^{\mathrm{th}}$ iteration as in (14). Then, update $\boldsymbol{u}^{(k)}$: $\boldsymbol{u}^{(k+1)}=\boldsymbol{u}^{(k)}+\Delta\boldsymbol{u}^{(k)}$.

$$\Delta\boldsymbol{u}^{(k)}=(\boldsymbol{S}_{Mu}^{y(k)})^{\mathrm{T}}[\boldsymbol{S}_{Mu}^{y(k)}(\boldsymbol{S}_{Mu}^{y(k)})^{\mathrm{T}}]^{-1}\Delta\boldsymbol{y}^{(k)} \tag{14}$$

*Step 5*: judge whether the active power of tie lines satisfies the convergence criterion of adjustment at the $k^{\mathrm{th}}$ iteration.

$$\Delta\boldsymbol{y}^{(k)}<\varepsilon_{AIML\text{-}in} \tag{15}$$

where $\varepsilon_{AIML\text{-}in}$ is the convergence coefficient of the adjustment. In this paper, $\varepsilon_{AIML\text{-}in}=10^{-4}$. If either (9) or (15) is not satisfied, repeat *Step 2* to *Step 5*, or calculate other required data and output the results.

The diagram of the steps of AIML-in is shown in Supplementary Material A Fig. SA2.

## IV. ASN-QMC for RCA by PEDs in Stochastic Scenarios

### A. Identification of Tie Line Exceeding Limits

$P_{\mathrm{t}(i_k\text{-}j_k)}^{\max}$ is the rated value of $P_{\mathrm{t}(i_k\text{-}j_k)}$. After PPF calculation, the sampling number, of which $p_{\mathrm{t}(i_k\text{-}j_k)}$ exceeds $P_{\mathrm{t}(i_k\text{-}j_k)}^{\max}$, is counted as $N_{\mathrm{t}(i_k\text{-}j_k)}$. The out-of-limit probability $p_{\mathrm{t}(i_k\text{-}j_k)}$ of tie line $i_k$-$j_k$ is:

$$p_{\mathrm{t}(i_k\text{-}j_k)}=N_{\mathrm{t}(i_k\text{-}j_k)}/N_{total} \tag{16}$$

where $N_{total}$ is the total number of samples. The average out-of-limit probability $\bar{p}_{\mathrm{t}}$ of tie lines is:

$$\bar{p}_{\mathrm{t}}=\frac{\sum_{k=1}^{n_{\mathrm{t}}}p_{\mathrm{t}(i_k\text{-}j_k)}}{n_{\mathrm{t}}} \tag{17}$$

Equations (16) and (17) reveal the active power of the tie line exceeding the limits in AC/DC systems with PEDs.

### B. Probabilistic Method Theory

#### 1) Introduction to ASN-QMC

The QMC uses low-difference sequences, e.g., Halton sequence, Sobol sequence, to generate samples [31]. Compared with MCS, QMC produces more uniformly distributed samples, resulting in fewer required samples. Specifically, for a given sampling number $N$, the convergence rate of QMC is $O(1/N)$, while that of MCS is only $O(1/\sqrt{N})$ [31]. Besides, the low-difference sequence used in QMC is deterministic and replicable, eliminating such randomness. As the sampling number increases, previously obtained results remain valid, and there is no need to re-sample. Given these advantages, the ASN-QMC is suitable to be adopted for the determination of the appropriate sampling number.

#### 2) Procedure of ASN-QMC

The Sobol sequence generates a sample set matrix $\boldsymbol{R}_{M\times N}$ with dimension $M$ and sampling number $N$ herein [36]. The data in each dimension of $\boldsymbol{R}_{M\times N}$ follow the uniform distribution over [0,1]. The sample set matrix $\boldsymbol{Z}_{M\times N}$ that follows the standard normal distribution can be obtained as:

$$\boldsymbol{Z}_{M\times N}=G^{-1}(\boldsymbol{R}_{M\times N}) \tag{18}$$

where $G$ is the cumulative distribution function of the standard normal distribution.

The Spearman correlation coefficient matrix amongst input variables is assumed to be $\boldsymbol{R}_x$. Since the Spearman correlation coefficient remains unchanged when such multidimensional arbitrary distribution is transformed to the standard normal distribution, the ements of the Pearson correlation coefficient matrix $\boldsymbol{R}_z$ amongst the variables that follow the normal distribution are given as:

$$\rho_{i,j}=2\sin\left(\frac{\pi}{6}\rho_{si,j}\right) \tag{19}$$

where $\rho_{i,j}$ and $\rho_{si,j}$ are the $i^{\mathrm{th}}$-row $j^{\mathrm{th}}$-column elements in $\boldsymbol{R}_z$ and $\boldsymbol{R}_x$, respectively. The sample set matrix $\boldsymbol{Z}'_{M\times N}$ following the standard normal distribution with the desired correlation is given as:

$$\boldsymbol{Z}'_{M\times N}=\boldsymbol{L}\boldsymbol{Z}_{M\times N} \tag{20}$$

where $\boldsymbol{L}$ satisfies $\boldsymbol{R}_z=\boldsymbol{L}\boldsymbol{L}^{\mathrm{T}}$.

Based on the cumulative distribution function $F_X$ of the probability distribution followed by each random input variable (named original distribution), the sample set matrix $\boldsymbol{X}_{M\times N}$ of the inputs, can be determined as:

$$\boldsymbol{X}_{M\times N}=F_X^{-1}(G(\boldsymbol{Z}'_{M\times N})) \tag{21}$$

where $F_X^{-1}$ is the inverse function of $F_X$.

Based on $\boldsymbol{X}_{M\times N}$, $N$ times of DPFs are calculated, and the output sample set matrix $\boldsymbol{Y}_{M\times N}$ of DPF can be obtained. The PPF result $\boldsymbol{Y}_{PPF}$, such as the standard deviation $\sigma_{\boldsymbol{Y}}$ of $\boldsymbol{Y}_{M\times N}$, can be calculated as $\boldsymbol{Y}_{PPF}=h(\boldsymbol{Y}_{M\times N})$, where $h$ is the PPF function that processes $\boldsymbol{Y}_{M\times N}$.

To balance the computational accuracy and efficiency, the ASN-QMC can be used to find an appropriate sampling number $N$. In ASN-QMC, an initial sampling number $N_0$ is set. The change step of the sampling number is denoted as $\Delta N$. After $i$ increments, the total sampling number $N_i$ equals $N_0+\Delta N_i$. Due to the nature of the Sobol sequence, the results of new PPF calculations ($\Delta N$ samples) leave no effect on the previous calculation results. Therefore, the result $\boldsymbol{Y}_{PPF}$ of PPF calculation after $i$ changes is:

$$\boldsymbol{Y}_{PPF}=h([\boldsymbol{Y}_{M\times N_{i-1}},\boldsymbol{Y}_{M\times\Delta N}]) \tag{22}$$

The PPF calculation ends when the following criteria are satisfied:

$$\begin{cases}\Delta^2\sigma_{\boldsymbol{Y}(N_i)}=\left|\sigma_{\boldsymbol{Y}(N_i)}-2\sigma_{\boldsymbol{Y}(N_{i-1})}+\sigma_{\boldsymbol{Y}(N_{i-2})}\right|<\varepsilon_{ASN\text{-}QMC}\\ \Delta^2\bar{p}_{\mathrm{t}(N_i)}=\left|\bar{p}_{\mathrm{t}(N_i)}-2\bar{p}_{\mathrm{t}(N_{i-1})}+\bar{p}_{\mathrm{t}(N_{i-2})}\right|<\varepsilon_{out\text{-}of\text{-}limit}\end{cases} \tag{23}$$

where $\sigma_{\boldsymbol{Y}(N_i)}$ and $\bar{p}_{\mathrm{t}(N_i)}$ denote $\sigma_{\boldsymbol{Y}}$ and $\bar{p}_{\mathrm{t}}$ when the sampling number is $N_i$, respectively; $\Delta^2\sigma_{\boldsymbol{Y}(N_i)}$ and $\Delta^2\bar{p}_{\mathrm{t}(N_i)}$ denote the backward second-order differences of $\sigma_{\boldsymbol{Y}}$ and $\bar{p}_{\mathrm{t}}$, respectively; and $\varepsilon_{ASN\text{-}QMC}$ and $\varepsilon_{out\text{-}of\text{-}limit}$ are the convergence coefficients, of which the values significantly determine the efficiency and accuracy of ASN-QMC, respectively. The small values of $\Delta^2\sigma_{\boldsymbol{Y}(N_i)}$ and $\Delta^2\bar{p}_{\mathrm{t}(N_i)}$ indicate the marginal changes in $\sigma_{\boldsymbol{Y}}$ and $\bar{p}_{\mathrm{t}}$, respectively.

### C. Procedure of RCA in Stochastic Scenarios

The RCA by PEDs can effectively mitigate the risk of the system in stochastic scenarios and reveal the system operation status after the adjustment of PEDs. Moreover, the ANS-QMC is used for sampling and PPF calculation. For each sample, AIML is applied to calculate the DPF of the AC/DC system with PEDs, and RCA by PEDs is used to reduce out-of-limit probability. The whole procedure is illustrated in Fig. 4.

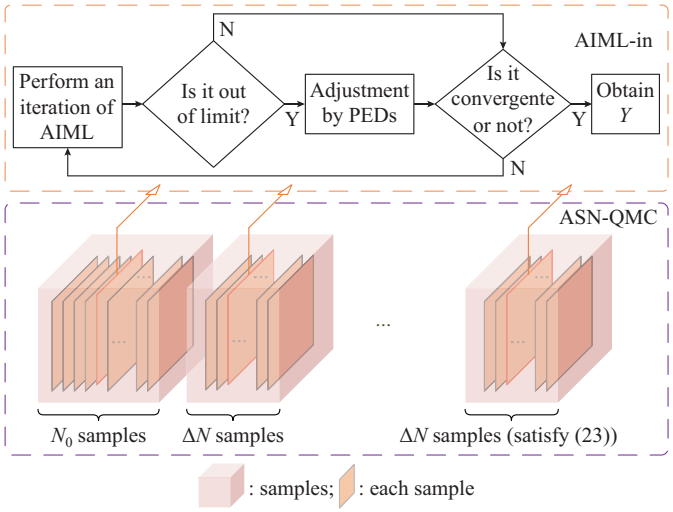


Fig. 4. Diagram of RCA by PEDs in stochastic scenarios.

## V. Case Study

### A. Test Systems Under Study

1) Case A: three different test systems are designed to verify the performance of AIML, i. e., case A1: IEEE 14-bus system; case A2: IEEE 57-bus system; and case A3: IEEE 118-bus system. Only the local adjustment of PEDs is considered. The control parameters of PEDs are detailed in Supplementary Material A Table SAII. The AC system test cases for IEEE standards are sourced from the MATPOWER [37]. The basic parameters for PEDs, e. g., equivalent impedance, control coefficient, are sourced from [12], [14], and [34].

2) Case B: some uncertainties are added to case A3, which is used to verify the performance of ASN-QMC in the AC/DC system with PEDs. The data related to uncertainties are sourced from [38].

The active power of loads in area 1 and area 2 follows the normal distribution, of which the mean is equal to the corresponding active power in the original case, and the standard deviation is equal to 5% of the mean. The power factor of each load is fixed. There are three wind farms in this system. The location and number of wind turbines, as well as the Spearman correlation coefficient matrix of wind in each wind farm, are shown in Fig. 5.

The wind speeds follow the Weibull distribution with shape parameter and scale parameters equaling 3.97 and 10.7, respectively. The cut-in, rated, and cut-out speeds of the wind turbines are set to be 4 m/s, 15 m/s, and 25 m/s, respectively. The rated power of each wind turbine is 2 MW.

3) Case C: case C is designed to explain the characteristics of the RCA and the local adjustment of PEDs. Lines 23-24, 30-38, and 33-37 are the tie lines of two areas in Fig. 5, with rated active power of 1.1, 2.0, and 0.2 p.u., respectively. Assume $P^{ref}_{\mathrm{t}(23\text{-}24)}=0.13$ p. u., $P^{ref}_{\mathrm{t}(30\text{-}38)}=0.35$ p. u., and $P^{ref}_{\mathrm{t}(33\text{-}37)}=-0.15$ p.u.. The location and control parameters of PEDs are the same as those in case A3. Note that control parameter $P_{37\text{-}33}$ of GUPFC directly adjusts the active power of tie line 33-37, while in case C1, only $P_{37\text{-}33}$ of GUPFC, i.e., the local adjustment, is considered. Also, the RCA by PEDs is considered in case C2.

4) Case D: based on case B and case C1, to verify the performance of RCA by PEDs in stochastic scenarios, the probability of the active power of tie lines exceeding the limit is reduced as much as possible by the adjustments of PEDs.

All the tests are implemented in MATLAB 2023a [39] on a personal computer with Intel(R) Core(TM) i7-13700K CPU @ 3.40 GHz and 32 GB 6400 MHz DDR5.

### B. Case A: DPF for AC/DC System with PEDs

In this subsection, the performance of AIML in calculating the DPF of the AC/DC system with PEDs is studied. The results of UIM, AIM, and AIML are compared through case A, and the computational time of each method is discussed in detail. The convergence accuracy of the three methods is set to be $10^{-6}$.

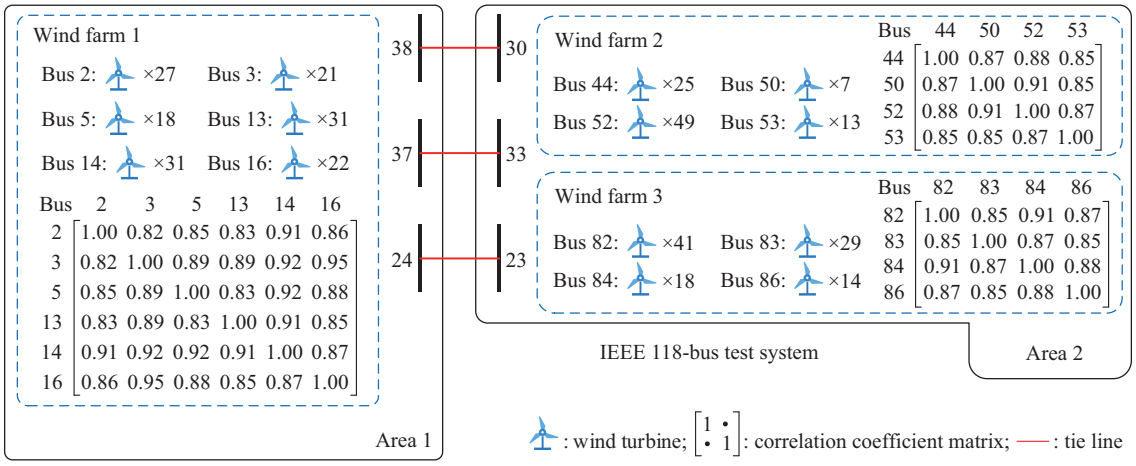


Fig. 5. Introduction to test system for case B and case C.

*1) Results of Power Flow Calculation*

The DPF results of bus voltage magnitude $V$ and phase angle $\theta$ of case A1 to case A3 among three methods with PEDs are shown in Fig. 6 and Fig. 7.

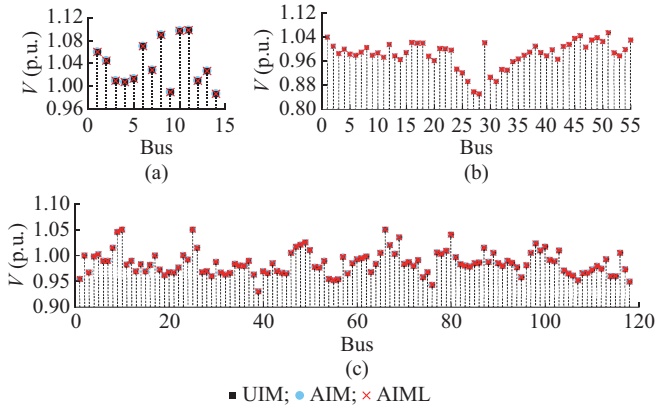


Fig. 6. DPF results of bus voltage magnitude in each case. (a) Case A1. (b) Case A2. (c) Case A3.

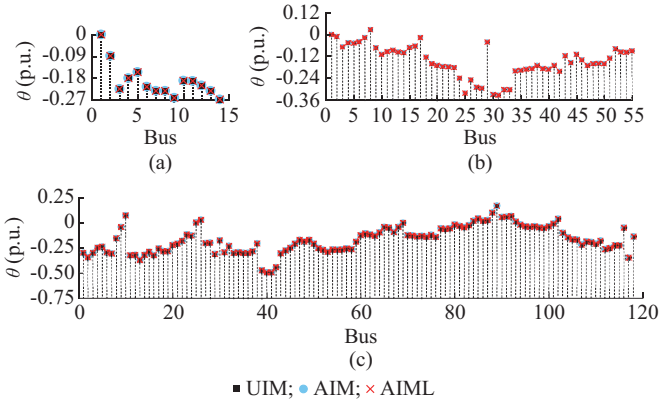


Fig. 7. DPF results of phase angle in each case. (a) Case A1. (b) Case A2. (c) Case A3.

In case A, the results of AIML are nearly identical to those of AIM and UIM under the same convergence accuracy, further demonstrating the feasibility and high accuracy of AIML for DPF calculation.

*2) Discussion on Computational Time*

Table I illustrates the computational time and iterations of the three methods in case A. AIML and AIM can be divided into three modules: AC, DC, and PEDs. The PED module includes four components: GUPFC (or UPFC), SSSC, STATCOM, and VSC. The number of iterations in each module at the $k^{\text{th}}$ iteration under case A using AIM are shown in Table II.

TABLE I
COMPARISON OF COMPUTATIONAL TIME AND ITERATIONS OF EACH METHOD

| Method | Case A1 | | Case A2 | | Case A3 | |
|---|---|---|---|---|---|---|
| | Time (s) | Iteration | Time (s) | Iteration | Time (s) | Iteration |
| AIML | 0.021 | 9 | 0.035 | 10 | 0.045 | 10 |
| AIM | 0.017 | 4 | 0.036 | 6 | 0.072 | 9 |
| UIM | 0.050 | 6 | 0.061 | 6 | 0.127 | 11 |

In case A, each module is calculated once in each iteration using AIML, implying that the iterations of each module are equivalent to the total iterations of AIML. According to Table I and Table II, it can be found that in case A1, not only the number of iterations of AIM is smaller than those of AIML ($4<9$), but also the sum of iterations per module is smaller than that of AIML (except for the VSC module), resulting in a little longer computational time of AIML compared with that of AIM. In case A2, although AIM has fewer iterations in total and the sum of iterations per module (except for the AC module) compared with AIML, the computational time of AIML is almost the same as that of AIM. The reason is that the AC module always has a greater computational burden than other modules, and AIM requires iterations in the AC module than AIML. In case A3, the test system is more complex, leading to increased iterations for both AIM and UIM. AIM achieves convergence in 9 iterations, as opposed to the 10 iterations required by AIML. Still, most of the sums of iterations per module are greater in AIM than those in AIML (except for the DC system), bringing shorter computational time of AIML compared with that of AIM. In addition, the computational time of UIM is always the longest in case A.

TABLE II
ITERATION IN EACH MODULE

| Case | The $k^{th}$ iteration | Iteration in each module | | | | | |
|---|---|---|---|---|---|---|---|
| | | AC | DC | GUPFC | SSSC | STATCOM | VSC |
| Case A1 | 1 | 3 | 2 | 4 | | 3 | 3 |
| | 2 | 1 | 1 | 1 | | 1 | 4 |
| | 3 | 1 | 0 | 1 | | 1 | 1 |
| | 4 | 0 | 0 | 0 | | 0 | 1 |
| | Sum | 5 | 3 | 6 | | 5 | 9 |
| Case A2 | 1 | 4 | 3 | 3 | 3 | 0 | 3 |
| | 2 | 2 | 1 | 2 | 2 | 4 | 3 |
| | 3 | 4 | 1 | 2 | 3 | 0 | 1 |
| | 4 | 2 | 1 | 1 | 1 | 0 | 1 |
| | 5 | 1 | 0 | 1 | 1 | 0 | 1 |
| | 6 | 1 | 0 | 1 | 0 | 0 | 0 |
| | Sum | 14 | 6 | 10 | 10 | 4 | 9 |
| Case A3 | 1 | 4 | 3 | 1 | 1 | 1 | 3 |
| | 2 | 3 | 2 | 4 | 4 | 3 | 6 |
| | 3 | 2 | 1 | 2 | 3 | 2 | 3 |
| | 4 | 2 | 1 | 2 | 3 | 2 | 2 |
| | 5 | 1 | 0 | 1 | 2 | 1 | 1 |
| | 6 | 1 | 0 | 1 | 2 | 1 | 1 |
| | 7 | 1 | 0 | 1 | 2 | 1 | 1 |
| | 8 | 0 | 0 | 0 | 1 | 1 | 0 |
| | 9 | 0 | 0 | 1 | 1 | 0 | 0 |
| | Sum | 14 | 7 | 13 | 19 | 12 | 17 |

In case A, AIML can deal with the DPF of the AC/DC system with PEDs. Compared with other DPF methods, AIML is more computationally efficient than UIM and AIM when the iterations of AIML are equal to or fewer than those of AIM. This advantage becomes particularly notable as the system scale increases.

### C. Case B: PPF for AC/DC System with PEDs

In case B, to demonstrate the performance of ASN-QMC, the sampling number is increased from 200 until the criterion in (27) is satisfied. $\varepsilon_{ASN\text{-}QMC}$ and $\varepsilon_{out\text{-}of\text{-}limit}$ are set to be $10^{-3}$, and the change step $\Delta N$ is set to be 100. The results of RS-MCS with $10^5$ samples (named RS-MCS-$10^5$) are used as the reference for other PPF methods. The MCS method based on Latin hypercube sampling (LHS-MCS) is used as a comparative method. The variation of $\Delta^2\sigma$, of which the active power of tie lines 23-24 and 30-38 is considered, and the variation of $\Delta^2\bar{p}_t$ is presented, as shown in Table III.

Table III indicates that the ASN-QMC converges when the sampling number is 1500, where $\Delta^2\sigma_{P_{23\text{-}24}}$, $\Delta^2\sigma_{P_{30\text{-}38}}$, and $\Delta^2\bar{p}_t$ are all less than $10^{-3}$. Since ASN-QMC can reuse the generated samples, there is no need to resample as the sampling number increases. Therefore, in the procedure of sampling number determination, only 1500 DPF calculations are sufficient in ASN-QMC. However, a minimum of $200+300+400+\ldots+1500=11900$ DPF calculations are required by LHS-MCS, which is not practical for finding an appropriate sampling number in practice. Besides, to further demonstrate the superiority of the ASN-QMC, several specific sampling numbers, e.g., 500, 1500, and 2500, are selected. Two indices are used to evaluate the accuracy of different methods.

TABLE III
VARIATION OF BACKWARD SECOND-ORDER DIFFERENCE WITH SAMPLING NUMBER IN CASE B

| Sampling number | $\Delta^2\sigma_{P_{23\text{-}24}}$ | $\Delta^2\sigma_{P_{30\text{-}38}}$ | $\Delta^2\bar{p}_t$ |
|---|---|---|---|
| 700 | $3.5\times10^{-3}$ | $6.3\times10^{-3}$ | $5.7\times10^{-3}$ |
| 800 | $2.3\times10^{-3}$ | $5.0\times10^{-3}$ | $6.0\times10^{-3}$ |
| 900 | $5.1\times10^{-3}$ | $6.6\times10^{-3}$ | $3.4\times10^{-3}$ |
| 1000 | $1.3\times10^{-3}$ | $3.0\times10^{-3}$ | $1.8\times10^{-3}$ |
| 1100 | $3.1\times10^{-3}$ | $3.5\times10^{-3}$ | $2.7\times10^{-3}$ |
| 1200 | $9.2\times10^{-4}$ | $1.7\times10^{-4}$ | $1.7\times10^{-3}$ |
| 1300 | $2.2\times10^{-5}$ | $1.2\times10^{-3}$ | $5.5\times10^{-4}$ |
| 1400 | $1.3\times10^{-3}$ | $1.7\times10^{-3}$ | $2.8\times10^{-4}$ |
| 1500 | $1.3\times10^{-4}$ | $2.8\times10^{-4}$ | $2.2\times10^{-4}$ |

1) Relative error (RE): RE measures the difference in computational accuracy between the PPF method and RS-MCS-$10^5$. A smaller difference indicates a higher accuracy of the PPF method. RE is defined as:

$$RE=\frac{\left|R_{test}-R_{RS\text{-}MCS\text{-}10^5}\right|}{R_{RS\text{-}MCS\text{-}10^5}}\times100\% \tag{24}$$

where $R_{test}$ denotes the result of PPF method to be tested; and $R_{RS\text{-}MCS\text{-}10^5}$ denotes the result of RS-MCS-$10^5$.

2) The error of out-of-limit probability (EOLP): EOLP measures the error of average probability of $P_{t(i_k\text{-}j_k)}$ of tie line exceeding the limit. EOLP is calculated by substituting $P_{t(i_k\text{-}j_k)}$ in (16) into (24).

The results of RE and EOLP of the active power of tie lines in case B are shown in Table IV. From Table IV, the RE of mean $\mu$ is small using both LHS-MCS and ASN-QMC, but the RE of standard deviation $\sigma$ using LHS-MCS is greater, which is more obvious when the sampling number remains small. EOLP obtained by LHS-MCS is also greater, indicating that ASN-QMC can better characterize the tail parts of the distribution, thus quantifying the probability of output exceeding the limit with higher accuracy.

TABLE IV
RESULTS OF RE AND EOLP OF ACTIVE POWER OF TIE LINE IN CASE B

| Sampling number | Index | Results of tie line 23-24 | | Results of tie line 30-38 | |
|---|---|---|---|---|---|
| | | LHS-MCS (%) | ASN-QMC (%) | LHS-MCS (%) | ASN-QMC (%) |
| 500 | RE of $\mu$ | 0.051 | 0.075 | 0.029 | 0.059 |
| | RE of $\sigma$ | 0.918 | 0.568 | 0.142 | 0.005 |
| | EOLP | 25.632 | 5.801 | 6.977 | 3.134 |
| 1500 | RE of $\mu$ | 0.012 | 0.034 | 0.016 | 0.030 |
| | RE of $\sigma$ | 1.078 | 0.469 | 0.166 | 0.527 |
| | EOLP | 18.989 | 1.786 | 5.768 | 3.809 |
| 2500 | RE of $\mu$ | 0.027 | 0.050 | 0.007 | 0.027 |
| | RE of $\sigma$ | 1.103 | 0.586 | 0.381 | 0.026 |
| | EOLP | 1.834 | 2.628 | 3.943 | 1.719 |

### D. Case C and Case D: Performance of RCA by PEDs

#### 1) Case C: Adjustment of PEDs in DPF

To illustrate the limitation of local adjustment, case C1 is designed, only considering control parameter $P_{37\text{-}33}$ of GUPFC, which can directly adjust the active power of tie line 33-37. Since the impact of $P_{37\text{-}33}$ of GUPFC on the active power of the remaining two tie lines is unclear, $P_{37\text{-}33}$ of GUPFC is changed around the opposite number of $P^{ref}_{t(33\text{-}37)}$=−0.15 p.u. (the power flow directions of $P_{37\text{-}33}$ and $P^{ref}_{t(33\text{-}37)}$ are opposite), i.e., $P_{37\text{-}33}$ of GUPFC is adjusted from 0.11 p.u. to 0.2 p.u.. The active power of tie lines and the absolute value of the difference from the target ($|\Delta \boldsymbol{y}|$) are shown in Fig. 8, where the light-colored bar chart denotes the actual calculated value, and the dark-colored bar chart denotes the difference between the actual value and the reference value.

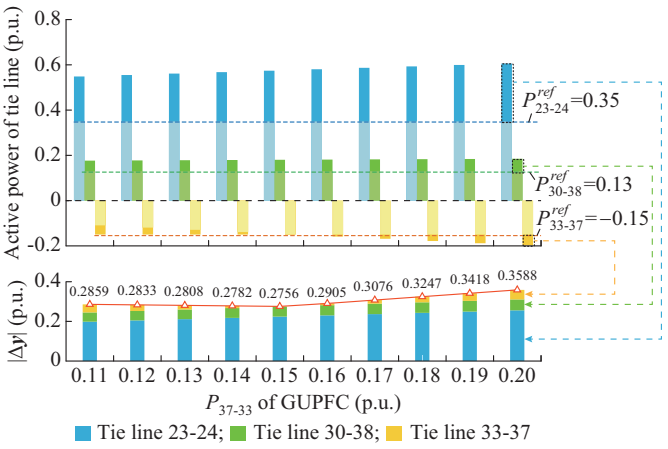


Fig. 8. Active power of tie lines and absolute value of difference from target ($|\Delta \boldsymbol{y}|$).

From Fig. 8, the minimum value of $|\Delta \boldsymbol{y}|$ is 0.2756 p.u. (which does not satisfy (15)) when $P_{37\text{-}33}$ of GUPFC is set to be 0.15 p.u., indicating that it is difficult to make the active power of tie lines reach the target only through the local adjustment by $P_{37\text{-}33}$ of GUPFC. Besides, as $P_{37\text{-}33}$ of GUPFC changes, the active power of tie line 33-37 is almost equal to the additive inverse of $P_{37\text{-}33}$ of GUPFC. However, an intuitive relationship between the active power of tie lines 23-24 and 30-38 and $P_{37\text{-}33}$ of GUPFC cannot be obtained. Therefore, it is unwise to change the active power of tie lines (PEDs are not adjacent) by local adjustments. Unless the control parameters of the PEDs are continuously and artificially modified after each DPF calculation, the effect of the adjustment of the PEDs on the desired target is ambiguous. As a result, it is essential to study the RCA to consider the ability of various PEDs to reach the target of all tie lines efficiently.

To verify the performance of RCA by PEDs using AIML combined with modular local sensitivity, case C2 is designed. In case A, AIM, AIML, and UIM can obtain the same DPF results, resulting in the same adjustment iterations of the three methods. However, the computational efficiency of AIM and AIML is mostly higher than that of UIM. Correspondingly, AIM-out and AIML-out have higher efficiency than UIM-out. Therefore, case C2 applies five methods, AIM-out, AIML-out, AIM-in, UIM-in, and AIML-in (proposed in this paper), not including UIM-out. Note that AIML-in adopts the modular local sensitivity, while other methods adopt the traditional local sensitivity. The changes of active power with adjustment iterations using different methods are shown in Fig. 9. From Fig. 9, the results reveal that all five methods can perform RCA by PEDs.

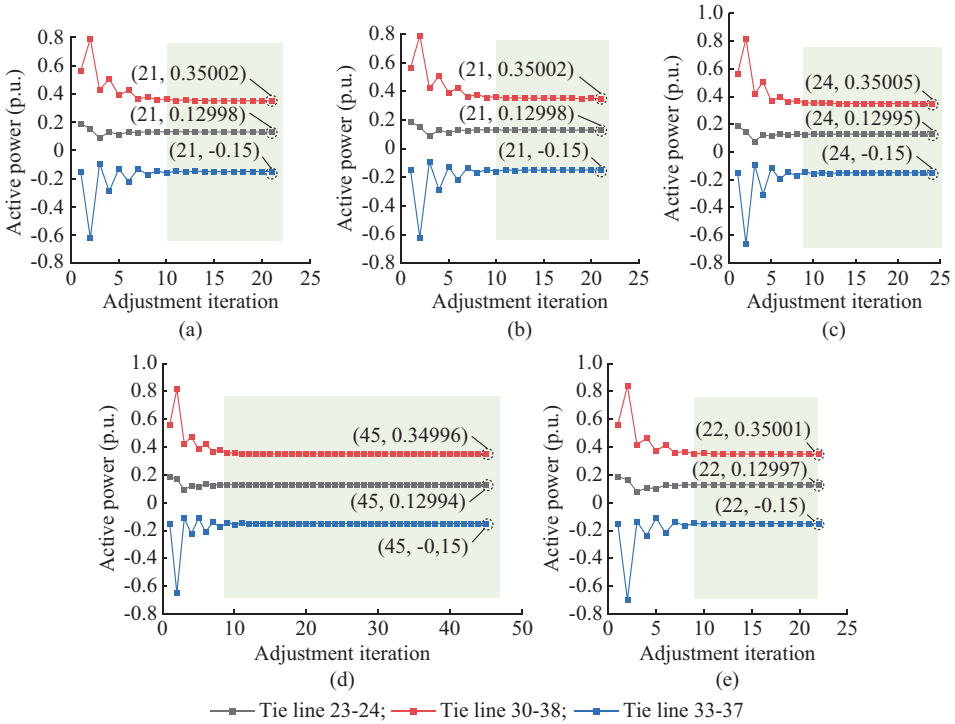


Fig. 9. Change in active power of tie lines with adjustment iterations in case C2 using different methods. (a) AIM-out. (b) AIML-out. (c) AIM-in. (d) UIM-in. (e) AIML-in.

From case A, the efficiency of DPF calculation in each adjustment iteration can be ranked as: AIM-out < AIML-out < UIM-in < AIM-in < AIML-in. The efficiency of sensitivity calculation can be ranked as: AIM-out = AIML-out = AIM-in < UIM-in ≈ AIML-in. Therefore, AIML-in achieves the highest efficiency in the DPF and sensitivity calculation. Besides, the AIML-in has only a total of 22 adjustment iterations, achieving the highest efficiency in performing RCA (0.53 s). Moreover, regardless of the method used, the green area in Fig. 9 indicates that some fine-tuning is required to satisfy the target under the same convergence criterion when $\varepsilon_{AIML\text{-}in}=10^{-4}$. If $\varepsilon_{AIML\text{-}in}$ is appropriately increased, fewer adjustment iterations can be achieved.

During the whole adjustment process, the absolute sum of modular local sensitivity $\sum|\boldsymbol{S}^{\boldsymbol{y}}_{\boldsymbol{Mu}}|$ using AIML-in is shown in Fig. 10, where the variable displayed on the *x*-axis denotes the set values of different control parameters of PEDs, and the PEDs which they belong to are shown in Supplementary Material A Table SAII. Since the target $\boldsymbol{y}$ in (13) denotes the active power of tie lines, which needs to be adjusted, the reactive power control parameters of PEDs have little effect on $\boldsymbol{y}$. This is evident from Fig. 10, where $\sum|\boldsymbol{S}^{\boldsymbol{y}}_{\boldsymbol{Mu}}|$ of the reactive power control parameters of each PED is relatively small. Additionally, it can be found that $\sum|\boldsymbol{S}^{\boldsymbol{y}}_{\boldsymbol{Mu}}|$ of $P_{37\text{-}33}$ is the largest. In fact, one of the GUPFC series sides directly controls the active power of tie line 33-37. As a result, the setting of $P_{37\text{-}33}$ exerts the most significant influence on the active power of this tie line.

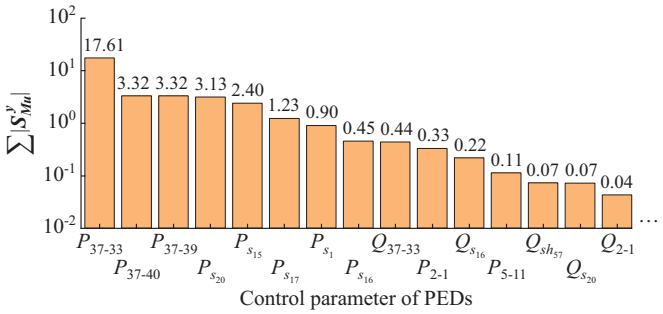


Fig. 10. $\sum|\boldsymbol{S}^{\boldsymbol{y}}_{\boldsymbol{Mu}}|$ in case C2.

*2) Case D: Adjustment of PEDs in PPF*

Similar to case B, the convergence criterion of ASN-QMC is satisfied when the sampling number is 1500 in case D. The installations of PEDs are the same as those of case C. The target value of the active power of tie lines is set to the rated active power minus 0.1 p.u.. The control parameters of PEDs are adjusted until the active power of all three tie lines is within their rated active power. Figure 11 illustrates the probability density functions (PDFs) of the active power of tie lines adjusted to reduce the out-of-limit probability with or without RCA.

The probabilities of active power exceeding the limit of tie lines 23-24 and 30-38 are 4.2% and 9.7%, respectively. After the RCA by PEDs, the out-of-limit probability is reduced. The blue line in Fig. 11 shows that the probability of the active power of tie lines 23-24 and 30-38 exceeding 1.1 and 2.0 p.u. is reduced.

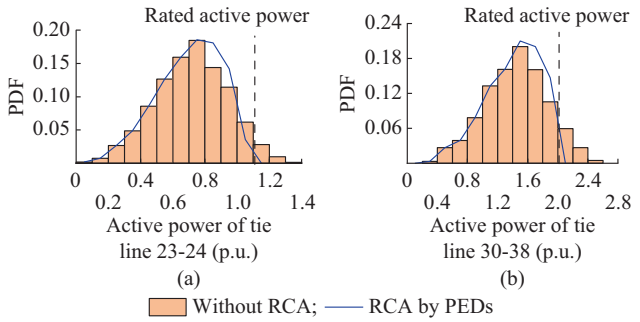


Fig. 11. PDFs of active power of different tie lines adjusted to reduce out-of-limit probability with or without RCA. (a) Tie line 23-24. (b) Tie line 30-38.

Besides, it can also be found that the heavy loading situation of each line has been alleviated.

The average values of $\Delta u$ and $\sum|\boldsymbol{S}^{\boldsymbol{y}}_{\boldsymbol{Mu}}|$ in case D are $\overline{\Delta\mu}$ and $\overline{\sum|\boldsymbol{S}^{\boldsymbol{y}}_{\boldsymbol{Mu}}|}$, which are available in Supplementary Material Table SAIII and Table SAIV, respectively. Similar to case C1, $\overline{\sum|\boldsymbol{S}^{\boldsymbol{y}}_{\boldsymbol{Mu}}|}$ of $P_{37\text{-}33}$ is the largest, as shown in Table SAIV. Meanwhile, for most of the active power control parameters, e.g., $P_{37\text{-}39}$, $P_{37\text{-}33}$, $P_{37\text{-}40}$, $\overline{\sum|\boldsymbol{S}^{\boldsymbol{y}}_{\boldsymbol{Mu}}|}$ is also larger. These parameters significantly impact $\boldsymbol{y}$, making them change significantly, as shown in Table SAIII. On the contrary, the reactive power control parameter of PEDs has a marginal effect on $\boldsymbol{y}$. The small values of $\overline{\sum|\boldsymbol{S}^{\boldsymbol{y}}_{\boldsymbol{Mu}}|}$ of reactive power of tie lines 94-93 and 94-95 and other reactive power control parameters indicate their limited influence on $\boldsymbol{y}$. These parameters show little change as can be observed from Table SAIII. In summary, the proposed RCA gives priority to the adjustment of control parameters of PEDs with high sensitivity, while taking into account all adjustable resources to prevent out-of-limit risk.

## VI. Conclusion

In this paper, the RCA of PEDs is studied to prevent the active power of tie lines from exceeding the limit in stochastic scenarios. The AIML is proposed to calculate the DPF of the AC/DC system with PEDs. The RCA of PEDs based on modular local sensitivity and AIML-in is proposed. The ASN-QMC is used to find an appropriate sampling number, thus balancing the accuracy and efficiency of PPF calculations. The performance of the proposed RCA is verified via four cases under the modified IEEE test systems.

In case A, AIML is compared with UIM and AIM in three cases, demonstrating that AIML can accurately calculate the DPF of the AC/DC system with PEDs. Moreover, the larger the system scale is, the higher the computational efficiency AIML achieves.

In case B, with the same sampling number, the PPF results of ASN-QMC are more accurate than those of LHS-MCS. Also, ASN-QMC adaptively determines an appropriate sampling number (1500 samples herein), effectively balancing the computational efficiency and accuracy.

In case C, based on modular local sensitivity and AIML-

in, the RCA is performed while considering the RCA ability of multiple PEDs. Besides, AIML-in has the highest computational efficiency compared with other methods.

In case D, the effectiveness of PEDs in stochastic scenarios is verified. Through RCA by PEDs, the probability of the active power of tie lines exceeding the limit is significantly reduced, thereby mitigating the risk in critical areas of the power system.

## REFERENCES


[1] L. Nan, T. Liu, and C. He, "Identification of transmission sections based on power grid partitioning," *International Transactions on Electrical Energy Systems*, vol. 29, no. 4, p. 2793, Dec. 2018.

[2] X. Wang, H. Wang, J. Yang *et al.*, "Application of 500 kV UPFC in Suzhou southern power grid," *The Journal of Engineering*, vol. 2019, no. 16, pp. 2580-2584, Jan. 2019.

[3] H. Zhou, Y. Su, Y. Chen *et al.*, "The China Southern Power Grid: solutions to operation risks and planning challenges," *IEEE Power and Energy Magazine*, vol. 14, no. 4, pp. 72-78, Jul. 2016.

[4] Y. S. Borovikov, A. S. Gusev, A. O. Sulaymanov *et al*., "A hybrid simulation model for VSC HVDC," *IEEE Transactions on Smart Grid*, vol. 7, no. 5, pp. 2242-2249, Sept. 2016.

[5] P. Tian, Y. Jin, N. Xie *et al*., "Power flow calculation for VSC-based AC/DC hybrid systems based on fast and flexible holomorphic embedding," *Journal of Modern Power Systems and Clean Energy*, vol. 12, no. 5, pp. 1370-1382, Sept. 2024.

[6] W. Wang and M. Barnes, "Power flow algorithms for multi-terminal VSC-HVDC with droop control," *IEEE Transactions on Power Systems*, vol. 29, no. 4, pp. 1721-1730, Jul. 2014.

[7] C. A. M. Ordóñez, A. Gómez-Expósito, G. E. M. Vinasco *et al*., "Optimal coordinated operation of distributed static series compensators for wide-area network congestion relief," *Journal of Modern Power Systems and Clean Energy*, vol. 10, no. 5, pp. 1374-1384, Sept. 2022.

[8] N. G. Hingorani, "Flexible AC transmission," *IEEE Spectrum*, vol. 30, no. 4, pp. 40-45, Apr. 1993.

[9] J. Reeve, G. Fahny, and B. Stott, "Versatile load flow method for multiterminal HVDC systems," *IEEE Transactions on Power Apparatus and Systems*, vol. 96, no. 3, pp. 925-933, May 1977.

[10] M. Baradar and M. Ghandhari, "A multi-option unified power flow approach for hybrid AC/DC grids incorporating multi-terminal VSC-HVDC," *IEEE Transactions on Power Systems*, vol. 28, no. 3, pp. 2376-2383, Aug. 2013.

[11] A. Nabavi-Niaki and M. R. Iravani, "Steady-state and dynamic models of unified power flow controller (UPFC) for power system studies," *IEEE Transactions on Power Systems*, vol. 11, no. 4, pp. 1937-1943, Nov. 1996.

[12] B. Fardanesh, B. Shperling, E. Uzunovic *et al.*, "Multi-converter FACTS devices: the generalized unified power flow controller (GUPFC)," in *Proceedings of IEEE 2000 PES Summer Meeting*, Seattle, USA, Jul. 2000, pp. 1020-1025.

[13] R. Chai, B. Zhang, J. Dou *et al*., "Unified power flow algorithm based on the NR method for hybrid AC/DC grids incorporating VSCs," *IEEE Transactions on Power Systems*, vol. 31, no. 6, pp. 4310-4318, Nov. 2016.

[14] Z. Fan, Z. Yang, K. Xie *et al*., "General steady-state modeling and linearization of power electronic devices in AC-DC hybrid grid," *IEEE Transactions on Power Systems*, vol. 36, no. 6, pp. 5746-5755, Nov. 2021.

[15] J. C. F. Pérez, F. E. Cerezo, and L. R. Rodríguez, "Linear power flow algorithm with losses for multi-terminal VSC AC/DC power systems," *IEEE Transactions on Power Systems*, vol. 37, no. 3, pp. 1739-1749, May 2022.

[16] H. Ergun, J. Dave, D. van Hertem *et al*., "Optimal power flow for AC-DC grids: formulation, convex relaxation, linear approximation, and implementation," *IEEE Transactions on Power Systems*, vol. 34, no. 4, pp. 2980-2990, Jul. 2019.

[17] Z. Yang, H. Zhong, A. Bose *et al.*, "Optimal power flow in AC-DC grids with discrete control devices," *IEEE Transactions on Power Systems*, vol. 33, no. 2, pp. 1461-1472, Mar. 2018.

[18] W. Xi, R. Wang, Y. Wang *et al.*, "A novel UPFC model and its convexification for security-constrained economic dispatch," *IEEE Transactions on Power Systems*, vol. 37, no. 6, pp. 4202-4213, Nov. 2022.

[19] R. Palma-Behnke, L. Vargas, J. R. Pérez *et al.*, "OPF with SVC and UPFC modeling for longitudinal systems," *IEEE Transactions on Power Systems*, vol. 19, no. 4, pp. 1742-1753, Nov. 2004.

[20] W. Chenlu, C. Feng, Y. Zeng *et al.*, "Improved correction strategy for power flow control based on multi-machine sensitivity analysis," *IEEE Access*, vol. 8, pp. 82391-82403, Jan. 2020.

[21] X. Fang, J. H. Chow, J. Xia *et al.*, "Sensitivity methods in the dispatch and siting of FACTS controllers," *IEEE Transactions on Power Systems*, vol. 24, no. 2, pp. 713-720, May 2009.

[22] S. Li, T. Wang, J. Xue *et al.*, "Control of active power loops in power system with UPFC based on power flow sensitivity," *Power System Technology*, vol. 42, no. 11, pp. 3768-3774, Nov. 2018.

[23] B. R. Prusty and D. Jena, "A critical review on probabilistic load flow studies in uncertainty constrained power systems with photovoltaic generation and a new approach," *Renewable and Sustainable Energy Reviews*, vol. 69, pp. 1286-1302, Mar. 2017.

[24] X. Deng, P. Zhang, K. Jin *et al.*, "Probabilistic load flow method considering large-scale wind power integration," *Journal of Modern Power Systems and Clean Energy*, vol. 7, no. 4, pp. 813-825, Jul. 2019.

[25] H. Yu, C. Y. Chung, K. P. Wong *et al.*, "Probabilistic load flow evaluation with hybrid Latin hypercube sampling and Cholesky decomposition," *IEEE Transactions on Power Systems*, vol. 24, no. 2, pp. 661-667, May 2009.

[26] M. Hajian, W. Rosehart, and H. Zareipour, "Probabilistic power flow by Monte Carlo simulation with Latin supercube sampling," *IEEE Transactions on Power Systems*, vol. 28, no. 2, pp. 1550-1559, May 2013.

[27] H. Zhu, L. Liu, T. Li *et al.*, "A novel algorithm of maximin Latin hypercube design using successive local enumeration," *Engineering Optimization*, vol. 44, no. 5, pp. 551-564, May 2012.

[28] F. A. C. Viana, G. Venter, and V. Balabanov, "An algorithm for fast optimal Latin Hypercube design of experiments," *International Journal for Numerical Methods in Engineering*, vol. 82, no. 2, pp. 135-156, Oct. 2009.

[29] Q. Wang, T. Nakashima, C. Lai *et al.*, "Modified algorithms for fast construction of optimal Latin-Hypercube design," *IEEE Access*, vol. 8, pp. 191644-191658, Jan. 2020.

[30] S. Peng, H. Chen, Y. Lin *et al.*, "Probabilistic power flow for hybrid AC/DC grids with ninth-order polynomial normal transformation and inherited Latin Hypercube sampling," *Energies*, vol. 12, no. 16, p. 3088, Aug. 2019.

[31] A. Singhee and R. A. Rutenbar, "Why quasi-Monte Carlo is better than Monte Carlo or Latin Hypercube sampling for statistical circuit analysis," *IEEE Transactions on Computer-Aided Design of Integrated Circuits and Systems*, vol. 29, no. 11, pp. 1763-1776, Nov. 2010.

[32] X. Xu and Z. Yan, "Probabilistic load flow calculation with quasi-Monte Carlo and multiple linear regression," *International Journal of Electrical Power & Energy Systems*, vol. 88, pp. 1-12, Jun. 2017.

[33] S. Fang, H. Cheng, and G. Xu, "A modified NATAF transformation-based extended quasi-Monte Carlo simulation method for solving probabilistic load flow," *Electric Power Components and Systems*, vol. 44, no. 15, pp. 1735-1744, Aug. 2016.

[34] T. Shu, X. Lin, S. Peng *et al.*, "Probabilistic power flow analysis for hybrid HVAC and LCC-VSC HVDC system," *IEEE Access*, vol. 7, pp. 142038-142052, Jan. 2019.

[35] Z. Fan, Z. Yang, J. Yu *et al.*, "Minimize linearization error of power flow model based on optimal selection of variable space," *IEEE Transactions on Power Systems*, vol. 36, no. 2, pp. 1130-1140, Mar. 2021.

[36] P. Bratley and B. L. Fox, "Algorithm 659," *ACM Transactions on Mathematical Software*, vol. 14, no. 1, pp. 88-100, Mar. 1988.

[37] R. D. Zimmerman, C. E. Murillo-Sánchez, and R. J. Thomas, "Matpower: steady-state operations, planning and analysis tools for power systems research and education," *IEEE Transactions on Power Systems,* vol. 26, no. 1, pp. 12-19, Feb. 2011.

[38] Q. Xiao, "Comparing three methods for solving probabilistic optimal power flow," *Electric Power Systems Research*, vol. 124, pp. 92-99, Mar. 2015.

[39] The MathWorks, Inc. (2024, Jan.). MATLAB version: 9.14.0 (R2023a). [Online]. Available: https://www.mathworks.com.


**Junzhou Wang** received the B.S. degree from China University of Petroleum (East China), Qingdao, China, in 2022. He is currently pursuing the Ph.D. degree in the School of Electrical Engineering, Chongqing University, Chongqing, China. His research interests include probabilistic power flow analysis, flexible AC transmission system (FACTS), and power system planning.

**Xingyu Lin** received the Ph. D. degree in electrical engineering from the School of Electrical Engineering, Chongqing University, Chongqing, China, in 2024. He is currently a Postdoctor in the School of Electrical Engineering, Chongqing University. His research interests include probabilistic modeling of uncertainty source in power system, advanced probabilistic power flow method, and neural network algorithm.

**Junjie Tang** received the Ph.D. degree in electrical engineering at the Institute for Automation of Complex Power Systems, E. ON Energy Research Center, RWTH Aachen University, Aachen, Germany, in 2014. He is currently an Associate Professor with State Key Laboratory of Power Transmission Equipment Technology, School of Electrical Engineering, Chongqing University, Chongqing, China. His research interests include complex uncertainty quantification analysis for power system, modeling of hybrid AC/DC grid, and application of machine learning in power system.

**Yuzhi Wang** is currently working toward the M.S. degree at the School of Electrical Engineering, Chongqing University, Chongqing, China. Her research interests include operational reserve optimization in power system and linearization of AC optimal power flow model for unit commitment.

**Guodong Huang** received the B.S. degree in electrical engineering and automation from China Agricultural University, Beijing, China, in 2009, the M.S. degree in power system and automation from China Agricultural University, in 2011. He is currently working as a Senior Engineer in China Electric Power Research Institute, Beijing, China. His research interests include power grid dispatching automation, power system economic dispatching, and electricity market.

**Dan Xu** received the B. S. and M. S. degrees in electrical engineering from China Agricultural University, Beijing, China, in 2007 and 2009, and the Ph. D. degree in electrical engineering from China Electric Power Research Institute, Beijing, China, in 2022. He is a Senior Engineer in China Electric Power Research Institute. His research interests include optimization operation of large-scale power system and renewable energy integration.